energies

MDPI

Article

Linear Active Disturbance Rejection Control of Grid-Connected Photovoltaic Inverter Based on Deviation Control Principle

Xuesong Zhou, Jiayao Wang * and Youjie Ma

School of Electrical and Electronic Engineering, Tianjin University of Technology, No. 391 Binshui West Road, Xiqing District, Tianjin 300384, China; zhaohanyu@email.tjut.edu.cn (X.Z.); eeliwei@email.tjut.edu.cn (Y.M.)
* Correspondence: 183125305@stud.tjut.edu.cn; Tel.: +86-188-2208-5686

Received: 16 June 2020; Accepted: 16 July 2020; Published: 23 July 2020



Abstract: Photovoltaic grid-connected power generation systems are easily affected by external factors, and their anti-interference performance is poor. For example, changes in illumination and fluctuations in the power grid affect the operation ability of the system. Linear active disturbance rejection control (LADRC) can extract the "summation disturbance" information from the system and eliminate the disturbance at the fastest speed by controlling the signal before it affects the final output of the system. In this paper, an improved linear ADRC based on the principle of deviation control is proposed, and the voltage outer loop is controlled by an improved LADRC. This improved LADRC takes the deviation between each state variable and its observed value as the regulation basis for each state variable of the linear extended state observer (LESO). Based on the analysis of the bode diagram in the frequency domain, it can be concluded that, compared with the unimproved LADRC, the new LADRC has better disturbance rejection performance. The simulation results show that the control performance of the new, improved LADRC is better than that of the unimproved LADRC under different operating conditions, and it has better stability performance and anti-disturbance performance.

Keywords: photovoltaic grid-connected power generation system; frequency domain analysis; linear ADRC; disturbance resistance; linear extended state observer

1. Introduction

In today's era, environmental pollution is becoming more and more serious, and environmental protection has become a concern of people; in particular, the question of how to reduce the emission of pollutants and how to save resources has become a hot topic. Most thermal power plants still use non-renewable energy sources such as coal, oil, and natural gas. The pollutants generated by these non-renewable energy sources account for the majority of air pollution [1–3]; with the increasingly serious energy crisis, solar energy is the most promising renewable energy source, and photovoltaic power generation has become one of the most used renewable energy power generation methods [4,5]. The development and utilization of photovoltaic power generation technology has received widespread attention in countries all over the world [6–8]. Photovoltaic power generation has the advantages of environmental protection, cleaning, and easy maintenance, but it is also easily affected by external environmental factors and has randomness and volatility. The photovoltaic grid-connected inverter is an important power electronic converter to realize direct current–alternating current (DC-AC) conversion [9–12]. The photovoltaic grid-connected inverter is the interface between the renewable energy power generation system and the power grid, and it plays a decisive role in grid-connected power generation. Some scientific research results show promise in the design and development of

control strategies to penetrate renewable energy into the smart grid [13–15]. The authors of [13] adopted a discrete optimization algorithm. The authors of [14] introduced a novel power scheduling method for solving the inherent random availability of renewable energy. The authors of [15] present the robust virtual inertia control of an islanded microgrid, considering the high penetration of renewable energy sources (RESs). The photovoltaic power generation system realizes power conversion and grid-connected operation through grid-connected inverters. The photovoltaic grid-connected inverter model is a nonlinear and strongly coupled system. The inverter output waveform contains a lot of harmonic components around the switching frequency. When the harmonic resonance between the power generation system and the power grid and the mutual coupling between multiple inverters occurs, the phenomenon of harmonic interaction will occur, which is not conducive to system stability. In order to make the grid-connected current or output voltage of the inverter meet the relevant standards, choosing the right control strategy is critical. In a grid-connected photovoltaic power generation system, the quality of grid-connected electrical energy and the operating efficiency of the photovoltaic system depend on whether the photovoltaic system has a good control effect. The good control effect of the photovoltaic system can ensure the smooth completion of the grid connection. Therefore, this issue has aroused widespread concern in scholars at home and abroad [16–19]. The most traditional control method of the photovoltaic grid-connected inverter is double closed-loop proportional integral (PI) control. However, because the control accuracy is often unable to meet the requirements, many scholars have proposed improvements. The authors of [20] adopt the traditional PI control method to control the inverter, but the stability of the system needs to increase the gain of the PI controller, and this control method cannot obtain a good control effect. The authors of [21] proposed a deadbeat control strategy: the main advantage of this control strategy is that it can eliminate the instantaneous disturbance, but the control effect for periodic disturbance is not satisfactory. The strategy of increasing the controller proposed in [22] makes the system more complicated. The authors of [23] proposed repetitive control. In this case, although the steady-state performance of the system is improved, there is a fundamental period delay in the dynamic response process.

Considering that the proportional-integral-derivative (PID) controller commonly used in the system in practical engineering lacks high control performance when the disturbance exists, Han Jingqing proposed an active disturbance rejection controller (ADRC) [24] based on modern control theory. The practical experience of PID, which dominates the industry, tells us that the design of the controller should be as simple and versatile as possible, that the parameters should be adjustable and they should not depend on the object model. ADRC satisfies all the above requirements and is applicable to any situation, from not knowing the object model to fully grasping the object model [25–28]. ADRC has natural decoupling capabilities. The so-called ADRC is able to actively extract the disturbance information from the input/output signal of the controlled object before the disturbance significantly affects the final output of the system, and it then uses the control signal to eliminate it as soon as possible, thereby greatly reducing its influence on the controlled quantity. The main points of the basic idea of ADRC include the following: standard type and total disturbance, expansion state and disturbance overall identification, differential signal generation and arrangement transition process and disturbance reduction and control quantity generation. Its core element is the extended state observer (ESO) [29]. The extended state observer observes and compensates the "total disturbance" in real time, so that the controlled object can be simplified into an integral tandem type. Han Jingqing pointed out that, as the simplest system, the integrator series system plays an important role in the design of the control system. The integrator series structure of the system is not only the standard structure of linear systems under linear feedback but also the standard structure of nonlinear systems under nonlinear feedback transformation. Many nonlinear systems can be linearized by nonlinear state feedback and become a series structure of integrators, thus simplifying the design of the controller. His deep understanding of the standard series of integral series allowed him to boldly contradict the artificial separation of linear and non-linear when further thinking about the control problem. He takes the integral series type as the standard type of the feedback system and unifies the

control problems of the linear stationary system and the nonlinear time-varying system. The creative contribution of ADRC lies in the proposition of standard and total disturbance concepts, expanding the total disturbance into a state of the system and using the state observer to identify its whole. ADRC has the advantages of strong robustness and a large controllable range, but the structure of this nonlinear control is more complicated, and the theoretical analysis is facing greater difficulties. At the same time, there are too many control parameters. The general form of the control parameter reaches 12, which is not conducive to engineering applications, and it is difficult to perform frequency domain analysis, commonly used in engineering to determine the stability boundary. On this basis, in view of the shortcomings of the original nonlinear ADRC, inspired by the time scale proposed by Han Jingqing, Gao Zhiqiang proposed the concept of frequency scale, and related the ADRC parameters to the frequency, making the physical significance of the parameters of the auto-disturbance controller more intuitive [30]. At the same time, all controllers and expanded state observers are implemented in a linear form, with controller bandwidth and observer bandwidth as their only parameters, and controller and expanded state observer parameter groups are constructed to reduce the controller parameters to three. This even provides the empirical relationship between the controller bandwidth and the observer bandwidth under general circumstances, which further simplifies the ADRC parameter tuning method. Gao Zhiqiang linearized the ADRC and proposed a linear active disturbance rejection controller (LADRC) which simplified the parameters and was more suitable for engineering applications.

This paper innovatively proposes an improved linear active disturbance rejection controller (LADRC) based on the error control principle: the adjustment process of each state variable in the traditional linear extended state observer (LESO) is analyzed and improved, and the voltage outer loop is controlled by this improved linear active disturbance rejection controller. Compared with the traditional linear expansion state observer, the improved linear extended state observer has higher observation accuracy, and the estimated value of the system state variable is closer to its true value. This improved method can better observe and eliminate disturbances and has better anti-disturbance performance. The frequency domain analysis method is used to analyze the convergence, tracking and anti-disturbance of the improved linear active disturbance controller and assess the stability of the improved LESO and LADRC. The anti-disturbance performance of this improved LADRC is verified by simulation under multiple working conditions. In this paper, the photovoltaic grid-connected inverter will be used as the control object. By first modeling the photovoltaic grid-connected inverter, and then through the park transformation, the mathematical model in the d and q rotating coordinate systems is obtained. Through a detailed introduction to LADRC, based on the basic principle of deviation control, an improved linear expansion state observer is proposed. In the frequency domain, the theoretical analysis of the improved LADRC is carried out. The bode diagram simulation shows that the new LADRC has better anti-interference performance than the unmodified LADRC. The stability of the new LADRC proposed in this paper is proven. Finally, through the comparison of the Matlab/Simulink simulation platform under multiple working conditions, it is verified that the improved LADRC has good control performance.

The overall structure of the paper is as follows. The article first models and analyzes the photovoltaic (PV) grid-connected inverter. Through the theoretical analysis of the model of the photovoltaic grid-connected inverter, the anti-disturbance paradigm of the photovoltaic grid-connected inverter is obtained. According to the anti-interference paradigm of photovoltaic inverters, the first-order LADRC is designed and introduced. On the basis of traditional linear active disturbance rejection control, an innovative linear active disturbance rejection controller based on the principle of deviation control is innovatively proposed. The frequency domain analysis method is used to analyze and compare the anti-disturbance performance of the traditional linear active disturbance controller and the improved linear active disturbance controller. Then, the improved extended state observer and linear active disturbance rejection controller are proven to be stable. Finally, through the simulation under multiple working conditions, the superiority of the improved linear active disturbance rejection controller is verified through the performance index.

2. Three-Phase Photovoltaic Grid-Connected Inverter Model and Traditional LADRC

This section will be divided into four parts for analysis. First, Xuesong Zhou modeled the photovoltaic (PV) array grid-connected inverter and obtained the mathematical model of the PV grid-connected inverter in the three-phase stationary coordinate system and the two-phase rotating coordinate system, which laid the foundation for the design of the controller. In the second part, Youjie Ma analyzed the control strategy of the three-phase grid-connected inverter and determined the double closed-loop control strategy adopted in this paper. In the third part, Jiayao Wang theoretically analyzed the traditional linear active disturbance rejection control, which provided a theoretical basis for the improved linear active disturbance rejection control proposed later. In the fourth part, the three authors have determined the LADRC control block diagram and anti-disturbance paradigm of the three-phase photovoltaic grid-connected inverter. Through the anti-disturbance paradigm, the first-order linear auto-rejection controller used in this paper is determined for control.

2.1. Circuit Topology of Three-Phase Photovoltaic Grid-Connected System

The two-stage photovoltaic grid-connected system includes DC/DC link and DC/AC link energy conversion. First, the direct current output by the photovoltaic array is converted by the DC/DC boost chopper circuit. Then, a DC/AC inverter is used to convert DC power to AC power for the purpose of grid connection. Figure 1 is the topology diagram of the two-stage photovoltaic grid-connected power generation system. In the two-stage system, the circuit topologies of the chopper and the inverter are different: the chopper realizes the maximum power point tracking, and the inverter realizes the photovoltaic grid-connected control. At present, the two-stage type has more applications, because the control system design is simpler than that of the single-stage type.

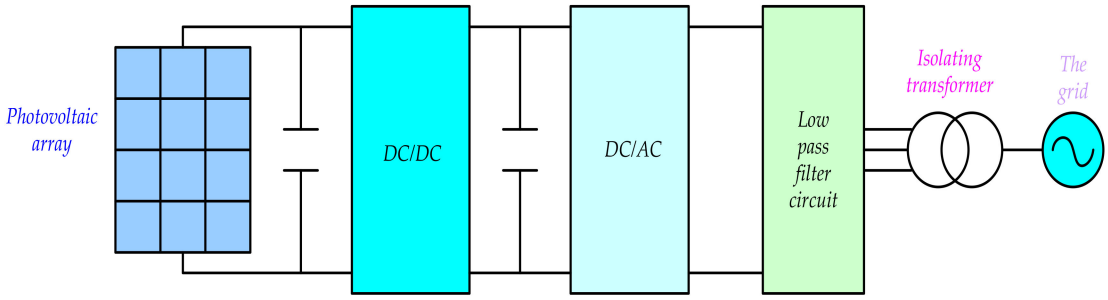

Figure 1. Topology diagram of two-stage grid-connected photovoltaic power generation system.

The photovoltaic grid-connected inverter is usually used as the interface device between the front-end DC/DC converter of the photovoltaic power generation system and the power grid. It is particularly important that the inverter is the core control link for low-voltage ride-through. When a voltage drop fault occurs in the power grid, the protection measures of the system rely on the inverter to achieve a solution. Therefore, it is necessary to analyze the mathematical model and control strategy of the inverter under normal conditions in detail. The quality of the output power of the photovoltaic power generation system mainly depends on the control performance of the grid-connected inverter. According to the different input methods, the photovoltaic grid-connected inverter can be divided into two types: voltage source type and current source type. Since the input method of the current source requires a large inductance in series on the DC side to stabilize the DC current, however, a large inductance in series will reduce the response speed of the system. Therefore, a voltage source type grid-connected inverter is often used in the industry. Figure 2 is the topology structure diagram of the photovoltaic grid-connected inverter, $L(\mu H)$ is the equivalent filter inductance, $R(\Omega)$ is the equivalent series resistance of the filter inductance, and $C(F)$ is the bus filter capacitance.

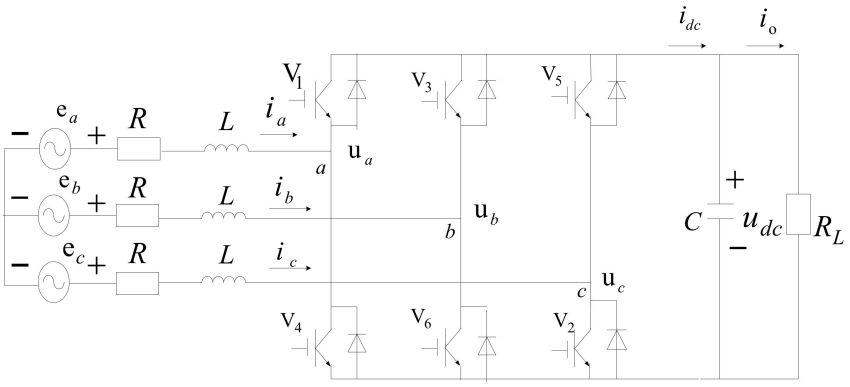

Figure 2. Topological structure diagram of photovoltaic grid-connected inverter.

According to Figure 2, in order to facilitate the analysis, the system model in the ideal state (excluding power consumption, switching dead zone and other factors) is established, and the current reference direction is taken, as shown in the figure. Combining Kirchhoff's law lists the AC side voltage equation as the following:

$$L\frac{d}{dt}\begin{bmatrix} i_a \\ i_b \\ i_c \end{bmatrix} = \begin{bmatrix} e_a \\ e_b \\ e_c \end{bmatrix} - R\cdot\begin{bmatrix} i_a \\ i_b \\ i_c \end{bmatrix} - \begin{bmatrix} u_a \\ u_b \\ u_c \end{bmatrix} \tag{1}$$

where i_a, i_b and i_c are the three-phase grid current (A), e_a, e_b and e_c are the three-phase grid voltage (V), and u_a, u_b and u_c are the grid-side inverter output phase voltage (V).

The connection mode of the photovoltaic power generation system is a three-phase three-wire system, which is a three-phase symmetrical system. From $e_a + e_b + e_c = 0$, $i_a + i_b + i_c = 0$, the mathematical model of the grid-connected photovoltaic inverter in the three-phase static coordinate system can be obtained:

$$\begin{cases} C\frac{du_{dc}}{dt} = \sum\limits_{i=a,b,c} i_i s_i - i_o \\ L\frac{di_i}{dt} + Ri_i = e_i - u_i \\ \sum\limits_{i=a,b,c} e_i = \sum\limits_{i=a,b,c} i_i = 0 \end{cases} \tag{2}$$

u_{dc}(V) is the voltage across the DC capacitor, i_{dc}(A) is the DC bus current. s_a, s_b and s_c are the components of the switching function on the abc axis, and i_o(A) is the output current of the pre-stage converter. It can be seen from Equation (2) that the mathematical model in the *abc* coordinate system is more complicated and needs to be further simplified in order to facilitate analysis. First, the variables of the *abc* coordinate system should be transformed to the $\alpha\beta$ coordinate system, and the transformation matrix should be selected [31]:

$$T_{clarke} = \frac{2}{3}\begin{bmatrix} 1 & -\frac{1}{2} & -\frac{1}{2} \\ 0 & \frac{\sqrt{3}}{2} & -\frac{\sqrt{3}}{2} \end{bmatrix} \tag{3}$$

The mathematical model in the $\alpha\beta$ coordinate system can be obtained by transforming Formula (2) through Formula (3):

$$\begin{cases} C\frac{du_{dc}}{dt} = \frac{3}{2}(i_\alpha s_\alpha + i_\beta s_\beta) - i_o \\ L\frac{di_\alpha}{dt} + Ri_\alpha = e_a - u_a \\ L\frac{di_\beta}{dt} + Ri_\beta = e_\beta - u_\beta \end{cases} \tag{4}$$

In the formula, i_α and i_β are the α-axis and β-axis current(A) components, e_α and e_β are the α-axis and β-axis grid voltage(V) components, u_α and u_β are the α-axis and β-axis inverter output voltage(V) components, and s_α and s_β are the components of the switching function on the α-axis and β-axis.

It can be seen from Equation (4) that the use of the $\alpha\beta$ coordinate system can simplify the mathematical model, but the formula still contains AC, which is not conducive to control. Therefore,

it is further transformed to convert the AC quantity of the $\alpha\beta$ coordinate system to the DC quantity of the dq coordinate system using the park transformation matrix [32]:

$$T_{park} = \begin{bmatrix} \sin\omega t & \cos\omega t \\ -\cos\omega t & \sin\omega t \end{bmatrix} \tag{5}$$

Equation (4) can obtain the mathematical model in the dq coordinate system after Park transformation:

$$\begin{cases} C\frac{du_{dc}}{dt} = \frac{3}{2}(i_d s_d + i_q s_q) - i_o \\ L\frac{di_d}{dt} = e_d - u_d + \omega L i_q - R i_d \\ L\frac{di_q}{dt} = e_q - u_q - \omega L i_d - R i_q \end{cases} \tag{6}$$

In the formula, e_d and e_q are the d-axis and q-axis grid voltage(V) components, i_d and i_q are the d-axis and q-axis current(A) components, u_d, u_q is the output voltage(V) of the inverter on the d-axis and q-axis, s_d and s_q are the d-axis and q-axis switching function components, and ω is the electrical angular velocity(rad/s). So far, the AC volume in the abc coordinate system has been transformed into a DC volume in the synchronous rotation dq coordinate system, which is more conducive to control analysis.

2.2. Control Strategy of Three-Phase Photovoltaic Grid-Connected Inverter

The three-phase photovoltaic grid-connected inverter must first ensure the stability of the DC bus voltage. The voltage loop control needs to be applied to the inverter, and the power control needs to be established by additionally establishing a current loop. Therefore, this paper adopts a double closed-loop control strategy of voltage outer loop and current inner loop. The current inner loop is divided into active current loop and reactive current loop. In order to realize the separation control of active power and reactive power, this is usually based on the grid voltage orientation (voltage-oriented control, VOC) vector control method. In the dq coordinate system, the d axis should be made to coincide with the grid voltage vector E, so as to obtain the grid voltage component in the dq coordinate system:

$$e_d = |E| \tag{7}$$

$$e_q = 0 \tag{8}$$

That is, the d-axis voltage is equal to the grid voltage amplitude, and the q-axis voltage is equal to zero. According to the instantaneous power theory [33], the active power P(W) and reactive power Q(W) of the inverter output are as follows:

$$P = \frac{3}{2}(i_d e_d + i_q e_q) \tag{9}$$

$$Q = \frac{3}{2}(i_d e_q - i_q e_d) \tag{10}$$

From Equations (7)–(10):

$$P = \frac{3}{2} i_d e_d \tag{11}$$

$$Q = -\frac{3}{2} i_q e_d \tag{12}$$

It can be seen that the output active power of the inverter is proportional to e_d and i_d. During grid-connected operation, e_d can be regarded as a fixed value, so controlling i_d can control active power. Similarly, the reactive power can be controlled independently through i_q. The calculation

usually does not consider the AC side filter and switching device losses, which can be obtained from the principle of conservation of active power on the DC side and AC side of the inverter:

$$P_{dc} = u_{dc} i_{dc} = \frac{3}{2} i_d e_d \tag{13}$$

The control structure of the PV grid-connected inverter is shown in Figure 3. In the photovoltaic grid-connected inverter control structure, a phase-locked loop (PLL) is used. Several scientific studies have shown further viable options for the PLL approach [34,35]. The authors of [34] introduce the design and implementation of a new programmable phase control unit (PCU) topology for active phased array antennas; the array is based on a hybrid direct digital synthesizer (DDS) phase-lock-loop (PLL) approach. The authors of [35] introduce the design and implementation of a high performance, reconfigurable, four channel beam steering unit (BSU) for active phased-array antennas based on field programmable gate array (FPGA) synthesized delay-lines and PLLs. In the photovoltaic power generation system, the DC power emitted by the photovoltaic cells must be converted into AC power through the inverter, so that it follows the frequency and phase of the grid current and meets the grid connection conditions before it can enter the grid. A phase-locked loop (PLL) is a closed-loop phase control system that is commonly used to track the frequency and phase of input signals to synchronize external input signals with target signals. In this series of processes, the setting of the phase-locked loop can enable the sinusoidal signal output by the inverter to track the grid voltage frequency and phase, thereby achieving the grid connection conditions, ensuring the smooth operation of the grid connection and also ensuring the stability of the system. In a photovoltaic grid-connected system, the phase-locked loop's phase-locked accuracy directly affects the system's grid-connected operating performance. The role of phase-locking technology in photovoltaic grid-connected systems is to make the grid voltage and inverter output current achieve synchronous phase-locking. The key is to track the grid voltage frequency and phase—that is, frequency and phase modulation. For the active link, it can be seen from Equation (13) that the DC voltage u_{dc} can be controlled by i_d, so the output of the DC voltage outer loop can be used as the reference value of i_d. First, the DC voltage u_{dc} should be collected and compared to the DC voltage given value u_{dc}^* with u_{dc} to obtain the error signal, and then the output is obtained as the d-axis current inner loop command value i_d^* through the ADRC regulator. For the reactive link, in order to achieve unit power factor control—that is, to control the reactive power to zero—$i_q^* = 0$ should be set by Formula (12). Finally, the current inner loop command values i_d^* and i_q^* are compared with the current actual values i_d and i_q, respectively. After the PI regulator and the coordinate inverse transformation link, the modulation signal in the *abc* three-phase coordinate system can be obtained, and the modulation signal sinusoidal pulse width modulation (SPWM) module can be used to obtain the driving signal of the switching device.

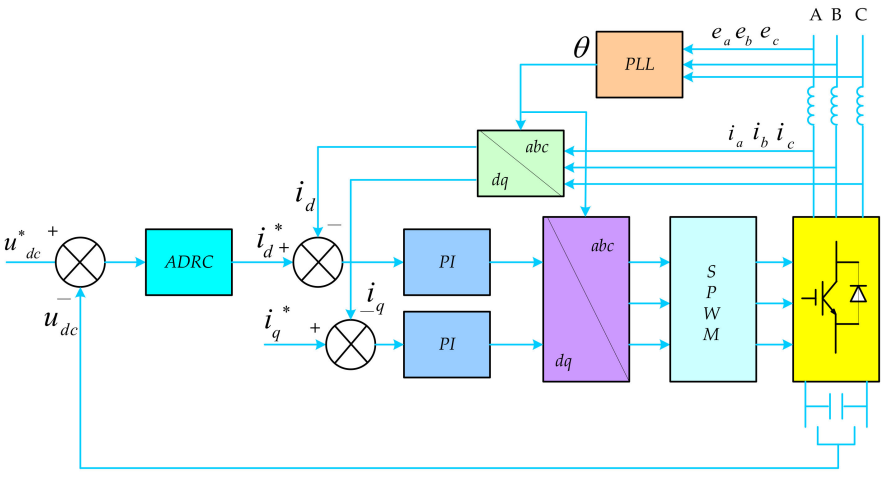

Figure 3. Control structure diagram of photovoltaic grid-connected inverter.

2.3. Traditional LADRC Control Structure

A LADRC consists of a linear tracking differentiator (LTD), linear expansion state observer (LESO) and linear state error feedback control rate (LSEF). Among them, LTD is used to arrange the transition process and solve the contradiction between rapidity and overshoot. LESO is the core part of LADRC. LESO expands the total disturbance into a new state variable of the system, and then uses the input and output of the system to reconstruct all states, including the original state variables and disturbances of the system which are output. LESF integrates the compensation of the interference estimator to generate the control signal. The traditional LADRC control block diagram is shown in Figure 4.

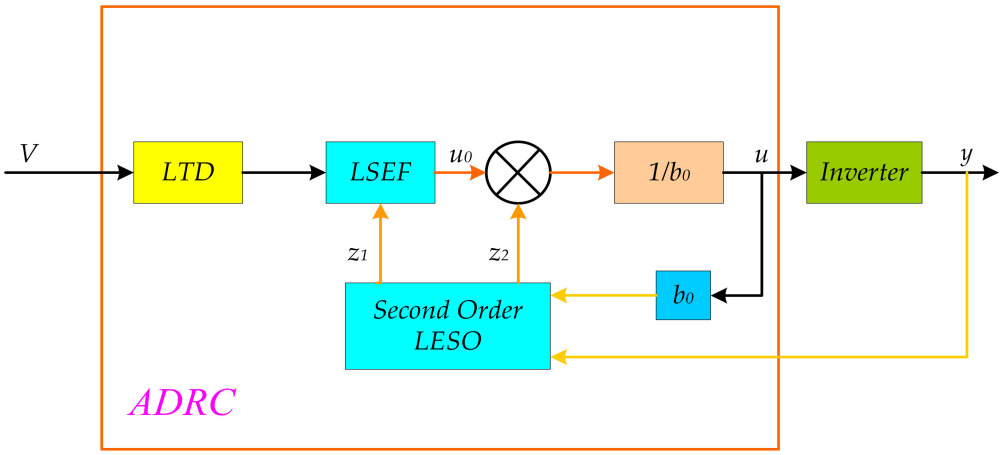

Figure 4. Structure of active disturbance rejection controller.

The main goal of ADRC linear simplification is factory-oriented engineering applications. The basic idea is to linearize the extended state observer (LESO) and connect its parameters to the observer bandwidth to simplify the design of the ESO; a simple PD control should be used for the combination, and the proportional coefficient and differential time constant should be linked with the bandwidth of the controller to simplify the tuning of the controller. LESO is the core structure of the linear auto-disturbance-rejection technology. By observing and estimating the total disturbance and providing compensation, the controlled system can be turned into a form of integrator in series and controlled, which improves the anti-disturbance performance of the system. Taking the first-order system as an example,

$$\dot{y} = -a_0 y + \omega + bu \tag{14}$$

where u is the input of the system, y is the output of the system, ω is the unknown disturbance of the system, a_0 is the parameter of the system, b is the part of the known input control gain (known part is b_0). Let $x_1 = y$, $x_2 = f(y, \omega) = -a_0 y + \omega + (b - b_0)u$, where x_1 is the output of the system, and x_2 contains all the uncertain factors of the system and the internal and external total disturbance of the system. Let $h = \dot{f}(y, \omega)$, then the equation of state of the first-order system can be described as follows:

$$\begin{cases} \begin{bmatrix} \dot{x}_1 \\ \dot{x}2 \end{bmatrix} = \begin{bmatrix} 0 & 1 \\ 0 & 0 \end{bmatrix} \begin{bmatrix} x_1 \\ x_2 \end{bmatrix} + \begin{bmatrix} b_0 \\ 0 \end{bmatrix} u + \begin{bmatrix} 0 \\ 1 \end{bmatrix} h \\ y = \begin{bmatrix} 1 & 0 \end{bmatrix} \begin{bmatrix} x_1 \\ x_2 \end{bmatrix} \end{cases} \tag{15}$$

The corresponding second-order ESO of the system is as follows:

$$\begin{cases} e = z_1 - y \\ \begin{bmatrix} \dot{z}_1 \\ \dot{z}_2 \end{bmatrix} = \begin{bmatrix} -\beta_1 & 1 \\ -\beta_2 & 0 \end{bmatrix} \begin{bmatrix} z_1 \\ z_2 \end{bmatrix} + \begin{bmatrix} b_0 & \beta_1 \\ 0 & \beta_2 \end{bmatrix} \begin{bmatrix} u \\ y \end{bmatrix} \end{cases} \tag{16}$$

In Equation (16), z_1 and z_2 are the state variables of the linear expansion state observer, z_1 is the tracking signal outputting y, z_2 is the tracking signal of the total system disturbance, and β_1 and β_2 are the output error correction gains. By choosing appropriate parameters, the state variables of the observer can track the state variables of the system quickly.

The total disturbance of the system can be observed by expanding the state variables and design disturbance compensation links:

$$u = \frac{u_0 - f}{b_0} \tag{17}$$

When the observer's state variable z_2 can track the system sum disturbance f well, the system can be simplified as follows:

$$\dot{y} = x_2 + b_0 u = x_2 + (u_0 - f) \approx u_0 \tag{18}$$

For the first-order system, since there is no observation of the differential of the system state, LSEF uses proportional control, the control law is the following:

$$u_0 = k_p(v - z_1) \tag{19}$$

k_p is the proportional control gain, and the closed-loop transfer function of the system can be obtained from Equations (18) and (19):

$$G(s) = \frac{k_p}{s + k_p} \tag{20}$$

The pole configuration of the controller can be obtained by $k_p = \omega_c$. By choosing an appropriate proportional gain, the system can achieve stability.

For further parameterization, the characteristic equation of the second-order LESO, A-LC is as follows:

$$\left|sI - (A - LC)\right| = s^2 + \beta_1 s + \beta_2 \tag{21}$$

In the formula, I is the identity matrix. To facilitate calculation, all observer poles are configured at $-\omega_o$ (ω_o is the observer bandwidth):

$$s^2 + \beta_1 s + \beta_2 = (s + \omega_o)^2 \tag{22}$$

Therefore, the gain of the second-order LESO can be obtained as follows:

$$\begin{cases} \beta_1 = 2\omega_o \\ \beta_2 = {\omega_o}^2 \end{cases} \tag{23}$$

It can be seen that, through the above configuration, the first-order LADRC can be simplified to the controller bandwidth ω_c and the observer bandwidth ω_o, two adjustable parameters. By adjusting the appropriate parameters, the system can achieve a good control effect.

Since the addition of the LTD link will cause the system to appear in a high-frequency oscillation after entering a steady state, LADRC is composed of LESO and LSEF. According to Formulas (14), (16), (17) and (19), the block diagram of the first-order LADRC can be obtained, as shown in Figure 5.

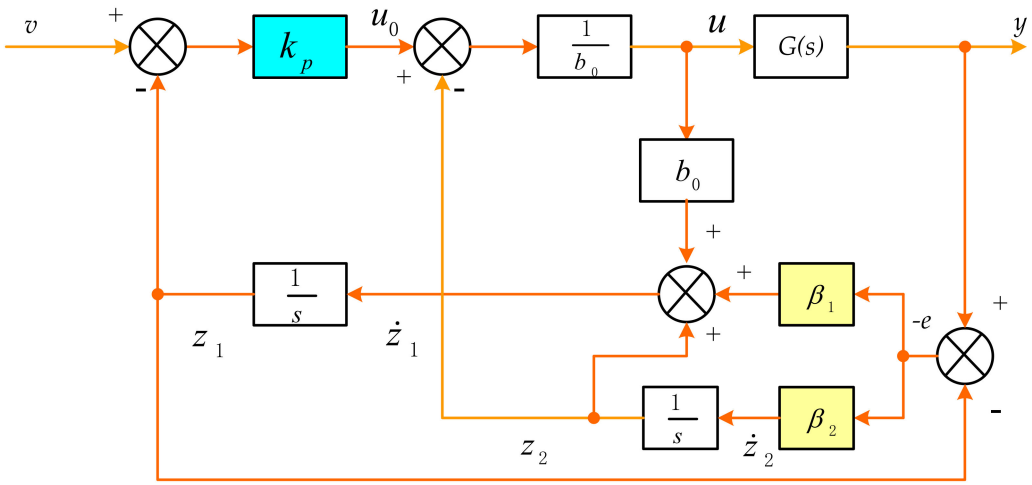

Figure 5. First-order linear active disturbance rejection control (LADRC) control block diagram.

2.4. Modeling and Design of Three-Phase Photovoltaic Inverter Based on LADRC

The mathematical model (6) of the three-phase photovoltaic grid-connected inverter in *dq* rotating coordinate system is transformed into the following:

$$\begin{cases} C\frac{du_{dc}}{dt} = i_{dc} - \frac{u_{dc}}{R_L} \\ L\frac{di_d}{dt} = -Ri_d + \omega Li_q + e_d - u_d \\ L\frac{di_q}{dt} = -Ri_q - \omega Li_d + e_q - u_q \end{cases} \tag{24}$$

Using LADRC to control the voltage outer loop, there are the following:

$$C\frac{du_{dc}}{dt} + \frac{u_{dc}}{R_L} = i_{dc} \tag{25}$$

According to Formula (13) and the conservation of active power of DC and AC measurements of photovoltaic inverters:

$$i_{dc} = 3e_d i_d / 2u_{dc} \tag{26}$$

Substituting Equation (26) into Equation (25) gives the following:

$$\frac{du_{dc}}{dt} = -\frac{u_{dc}}{R_L C} + \frac{3e_d i_d}{2C} \cdot \frac{1}{u_{dc}} \tag{27}$$

It is known from the equivalence of multiplication and addition that there must be a variable $\omega(t, u, x_1)$ such that $\frac{3e_d}{2C} i_d + \omega(t, u, x_1) = \frac{3e_d}{2C} i_d \cdot \frac{1}{u_{dc}}$, where u represents the control variable and x_1 represents the state variable that is the output variable. Then, Equation (27) can be equivalent to the following:

$$\frac{du_{dc}}{dt} = -\frac{u_{dc}}{R_L C} + \frac{3e_d i_d}{2C} + \omega(t, u, x_1) \tag{28}$$

Let the controlled output $y = x_1 = u_{dc}$, $b = \frac{3e_d}{2C}$, then $-\frac{u_{dc}}{R_L C}$ can be put into $\omega(t, u, x_1)$, and the above formula can be transformed into the following:

$$\dot{y} = \omega(t, u, x_1) + bi_d \tag{29}$$

Due to the double closed-loop control, the output of the voltage outer loop is used as the given value i_d^* (A) of the current inner loop—that is, the control quantity of the LADRC output—as follows:

$$\dot{y} = \omega(t, u, x_1) + bi_d^* \tag{30}$$

Let the total disturbance of the photovoltaic system $f(t,u,x_1) = \omega(t,u,x_1) + h(t)$, where $h(t)$ can be any external disturbance that the photovoltaic system may be subjected to, such as sudden changes in temperature and light. The anti-interference paradigm of photovoltaic grid-connected inverter is the following:

$$\begin{cases} \dot{y} = f(t,u,x_1) + bu \\ y = x_1 \end{cases} \tag{31}$$

From the previous analysis, it can be seen that the three-phase photovoltaic grid-connected inverter can be equivalent to a first-order system through theoretical analysis. When controlling it, a corresponding first-order LADRC (second-order LESO) control system needs to be designed.

LESO design of three-phase photovoltaic grid-connected inverter:

$$\begin{cases} e = z_1 - x_1 \\ \dot{z}_1 = z_2 - \beta_1 e + b i_d^* \\ \dot{z}_2 = -\beta_2 e \end{cases} \tag{32}$$

In the formula, z_1 is the observation value of x_1, which is the voltage state u_{dc}, and z_2 is the observation value of the internal and external total disturbance.

LSEF design of three-phase photovoltaic grid-connected inverter:

For the first-order system, LSEF adopts proportional control because it does not observe the differentiation of the system state. The p controller of the three-phase photovoltaic grid-connected inverter is as follows:

$$i_{d0} = k_p(u_{dc}^* - z_1) \tag{33}$$

where u_{dc}^*(V) is the given value of the DC bus voltage u_{dc}, k_p is the scale factor, and i_{d0}(A) is the proportional control rate. The disturbance compensation links are as follows:

$$u = i_d^* = \frac{(i_{d0} - z_2)}{b_0} \tag{34}$$

The LADRC control block diagram of the three-phase photovoltaic grid-connected inverter can be obtained from the Figure 6.

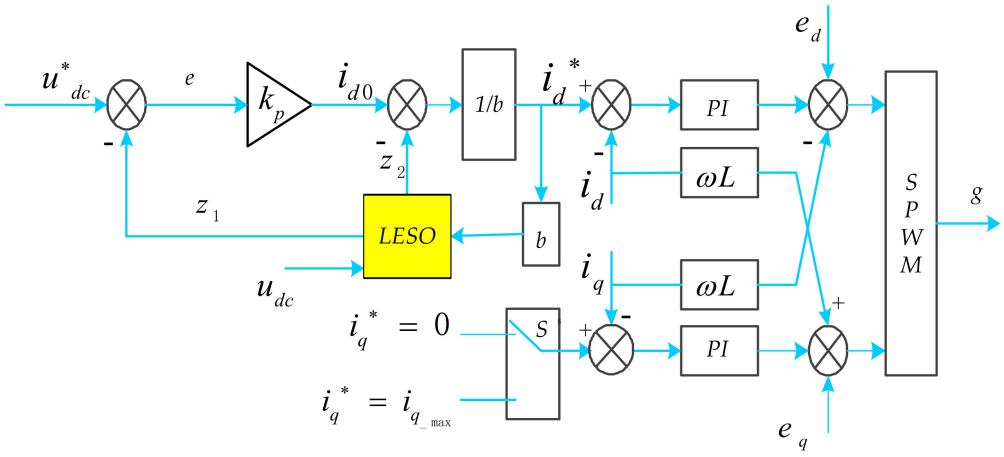

Figure 6. Control block diagram of photovoltaic grid-connected inverter based on LADRC.

It can be seen from the figure that the linear auto disturbance rejection controller omits the tracking differentiator, LSEF adopts proportional control, and ESO reduces the complexity of the system parameters during the adjustment process through linearization. This means that it is more suitable for engineering applications.

Converting Equation (32) into a transfer function:

$$\begin{array}{l} Z_1(s) = \frac{{\beta_2}^2+\beta_1 s}{(s+\frac{\beta_1}{2})^2} Y(s) + \frac{b_0 s}{(s+\frac{\beta_1}{2})^2} U(s) \\ Z_2(s) = \frac{\beta_2 s}{(s+\frac{\beta_1}{2})^2} Y(s) - \frac{b_0 \beta_2}{(s+\frac{\beta_1}{2})^2} U(s) \end{array} \tag{35}$$

Let the tracking error $e_1 = z_1 - y$, then:

$$e_1 = -\frac{s^2}{(s+\frac{\beta_1}{2})^2} y + \frac{s}{(s+\frac{\beta_1}{2})^2} b_0 u \tag{36}$$

Laplace transform on $f = x_2 = \dot{x}_1 - b_0 u = \dot{y} - b_0 u$ can obtain the following: $F(s) = sY(s) - b_0 U(s)$. The tracking error $e_2 = z_2 - f$ can be obtained as follows:

$$e_2 = (1 - \frac{\beta_2}{(s+\frac{\beta_1}{2})^2}) u b_0 - (1 - \frac{\beta_2}{(s+\frac{\beta_1}{2})^2}) s y \tag{37}$$

To facilitate error analysis, both y and u take a step signal with amplitude A, then $y(s) = \frac{A}{s}, u(s) = \frac{A}{s}$. From this, the steady-state error can be obtained:

$$\begin{cases} e_{1s} = \lim\limits_{s \to 0} s e_1 = 0 \\ e_{2s} = \lim\limits_{s \to 0} s e_2 = 0 \end{cases} \tag{38}$$

Through the above formula, we can conclude that the second-order LESO has very good convergence and can realize the error estimation of the photovoltaic system state variables and generalized disturbances.

3. Improved Second-Order LESO Design and Anti-Interference Analysis

3.1. Analysis and Design of Improved Second-Order LESO

The core of traditional LADRC is LESO, which is a typical application based on deviation control theory. Traditional ESO can control the changes of observed values in real time. This control method uses the deviation between the real value of the system state variable and the observed value of ESO to adjust. The ESO observation can produce a good estimate of the actual value. For traditional ESO, z_1 should be made to follow x_1 quickly, and then z_2 should be made to follow x_2. If the order is wrong, this adjustment method will have no effect, but the real system control method will not follow this order. When controlling z_1, the control of z_2 will also start synchronously; that is to say, the tracking of the observation value z_1 to x_1 has not reached the steady state, and it is very difficult to follow the observation value z_2 to x_2 of the total disturbance. Since z_1 follows x_1, the error e is already very small at this point, making it difficult for z_2 to adjust x_2. At this point, traditional ESO can only be achieved by selecting a larger parameter β, but larger parameters will affect the dynamic performance of ESO.

The above analysis shows that the traditional ESO adjusts the derivative of z_1 through e, which is in line with the error control principle. However, it is not suitable for adjusting the z_2 derivative.

For traditional first-order systems:

$$\dot{y} = f(y, \omega, t) + b_0 u \tag{39}$$

The corresponding equation of state is as follows:

$$\begin{cases} \dot{x}_1 = f + b_0 u \\ \dot{x}_2 = \dot{f} = h \\ y = x_1 \end{cases} \tag{40}$$

The corresponding traditional second-order LESO is as follows:

$$\begin{cases} e = z_1 - x_1 \\ \dot{z}_1 = z_2 - \beta_1 e + b_0 u \\ \dot{z}_2 = -\beta_2 e \end{cases} \tag{41}$$

According to Equation (41):

$$\begin{cases} z_1 = x_1 + e \\ z_2 = \dot{z}_1 + \beta_1 e - b_0 u \end{cases} \tag{42}$$

From Equations (40) and (41):

$$\begin{cases} z_1 = x_1 + e \\ z_2 = x_2 + \dot{e} + \beta_1 e \end{cases} \tag{43}$$

It can be seen that the error between z_2 and x_2 is $\dot{e} + \beta_1 e$, which is used as a new error to adjust the derivative of z_2.

The establishment of a new improved second-order LESO is as follows:

$$\begin{bmatrix} \dot{z}_1 \\ \dot{z}_2 \end{bmatrix} = \begin{bmatrix} -\beta_1 & 1 \\ 0 & -\beta_2 \end{bmatrix} \begin{bmatrix} z_1 \\ z_2 \end{bmatrix} + \begin{bmatrix} b_0 & \beta_1 & 0 \\ -b_0\beta_2 & 0 & \beta_2 \end{bmatrix} \begin{bmatrix} u \\ y \\ \dot{y} \end{bmatrix} \tag{44}$$

The block diagram of the improved LADRC control structure can be obtained as shown in Figure 7:

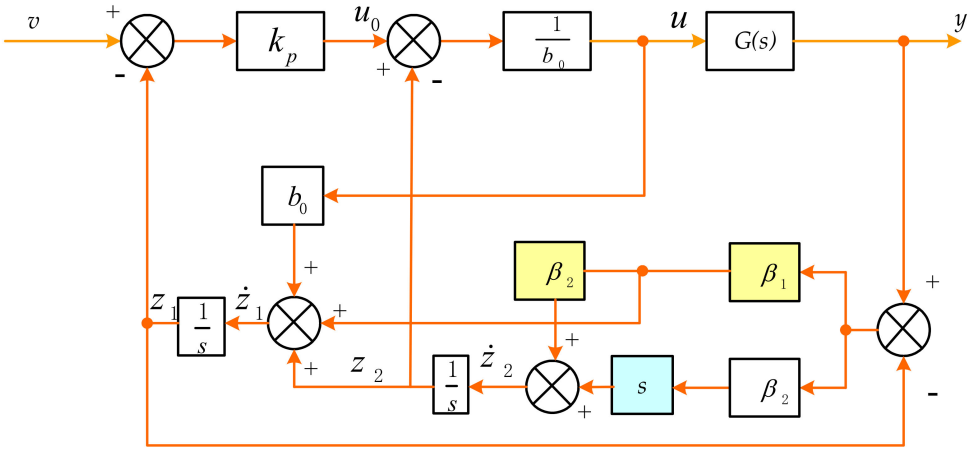

Figure 7. Block diagram of improved LADRC control structure.

Therefore, the improved LADRC system control model of the voltage outer loop of the three-phase photovoltaic grid-connected inverter can be obtained:

$$\begin{cases} e = z_1 - x_1 \\ \dot{z}_1 = z_2 - \beta_1 e + b i_d{}^* \\ \dot{z}_2 = -\beta_2 \left[(\dot{z}_1 - \dot{x}_1) + \beta_1 (z_1 - x_1) \right] \\ i_{d0} = k_p (u_{dc}{}^* - z_1) \\ i_d{}^* = \frac{(i_{d0} - z_2)}{b_0} \end{cases} \tag{45}$$

$i_d{}^*$ is the given value of the current inner loop formed by i_{d0} after "total disturbance" compensation. Converting (45) into the transfer function form gives the following:

$$\begin{cases} z_1 = \frac{\beta_1\beta_2+(\beta_1+\beta_2)s}{(s+\beta_1)(s+\beta_2)}y + \frac{b_0 s}{(s+\beta_1)(s+\beta_2)}u \\ z_2 = \frac{\beta_2 s}{s+\beta_2}y - \frac{b\beta 0_2}{s+\beta_2}u \end{cases} \tag{46}$$

Similarly, it can be proven that the improved second-order LESO has good convergence:

$$\begin{cases} e_{1s} = \lim\limits_{s\to 0} se_1 = 0 \\ e_{2s} = \lim\limits_{s\to 0} se_2 = 0 \end{cases} \tag{47}$$

3.2. Analysis and Design of Improved Second-Order LESO

From Equations (35) and (46), the transfer function of the observation noise δ_o of the traditional second-order LESO and the improved second-order LESO and the transfer function of the input disturbance δ_c can be obtained, respectively.

The traditional LESO noise transfer function is as follows:

$$\frac{z_1}{\delta_o} = \frac{2\omega_o s + {\omega_o}^2}{(s+\omega_o)^2} \tag{48}$$

The improved LESO noise transfer function is as follows:

$$\frac{z_1}{\delta_o} = \frac{2{\omega_o}^3 + (2\omega_o + {\omega_o}^2)s}{(s+2\omega_o)(s+{\omega_o}^2)} \tag{49}$$

Taking $\omega_o = 10$, it can be seen from the amplitude–frequency characteristic curve of the simulation in Figure 8 that the new ADRC has a significantly increased bandwidth compared with the traditional ADRC, and the phase lag of the middle frequency band has been significantly improved.

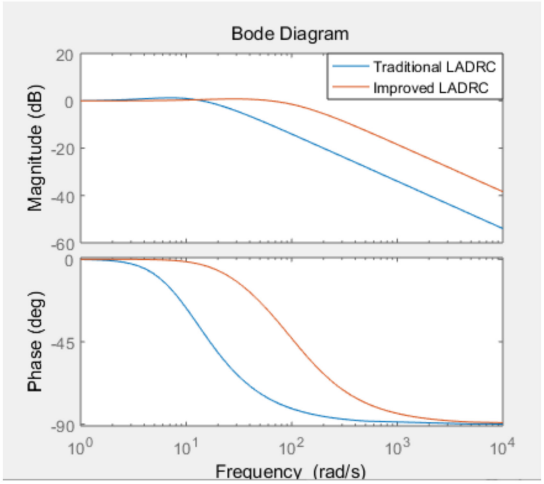

Figure 8. Comparative analysis of bode diagram of observed noise.

The transfer function of the disturbance δ_c at the input of the traditional LESO is as follows:

$$\frac{z_1}{\delta_c} = \frac{b_0 s}{(s+\omega_o)^2} \tag{50}$$

The transfer function of disturbance δ_c at the input of improved LESO is as follows:

$$\frac{z_1}{\delta_c} = \frac{b_0 s}{(s+{\omega_o}^2)(s+2\omega_o)} \tag{51}$$

As can be seen from the amplitude–frequency characteristic curve in Figure 9, the traditional LADRC and the improved LADRC are basically the same in high frequency band, but in the low frequency band, the improved LADRC has better anti-interference performance and a stronger ability to restrain input disturbance than the traditional LADRC.

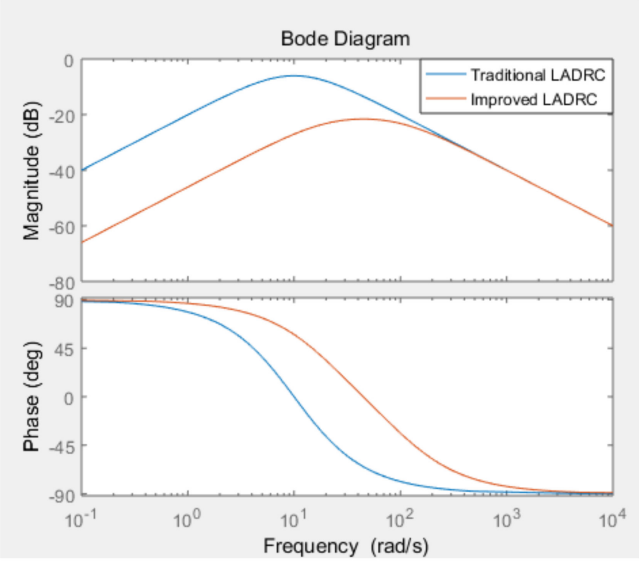

Figure 9. Comparative analysis of bode diagram of input disturbance.

For improved LADRC input perturbation δ_c transfer function, let $b_0 = 10$, $\omega_o = 10, 20, 30, 40, 50$. From the simulation graph in Figure 10's amplitude–frequency characteristic curve, it can be seen that the increase in ω_o has no effect on the high frequency band. However, the phase lag of the tracking input of the system decreases with the increase in the bandwidth of the improved LESO observer ω_o. The simulation shows that the improved LADRC can effectively suppress the input disturbance δ_c.

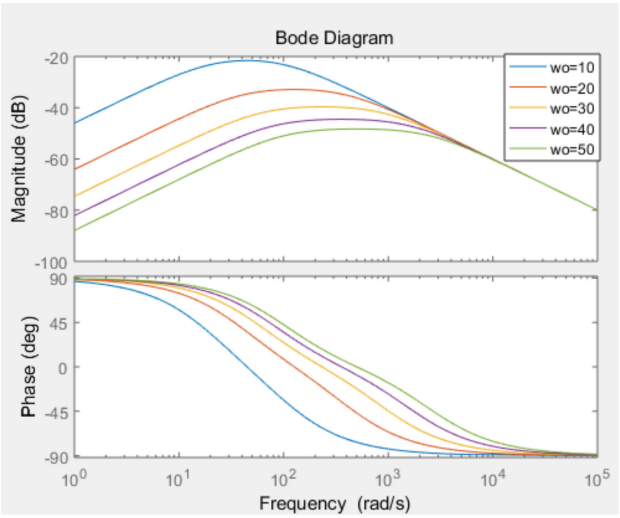

Figure 10. Bode diagram analysis of disturbance of the improved LADRC input terminal.

3.3. Analysis of Anti-Disturbance Performance of New LADRC in Actual System

According to Equation (45):

$$u = \frac{1}{b_0} G_1(s)(\omega_c u_{dc}{}^* - H(s)y) \tag{52}$$

Among them:

$$\begin{aligned} G_1(s) &= \frac{(s+\beta_1)(s+\beta_2)}{s^2+(\beta_1+\omega_c)s} \\ H(s) &= \frac{\beta_1\beta_2\omega_c+(\beta_1\beta_2+\beta_1\omega_c+\beta_2\omega_c)s+\beta_2 s^2}{(s+\beta_1)(s+\beta_2)} \end{aligned} \tag{53}$$

Then, (52) can be obtained based on the improved LADRC voltage loop simplified control system structure block diagram, which is shown in the following Figure 11:

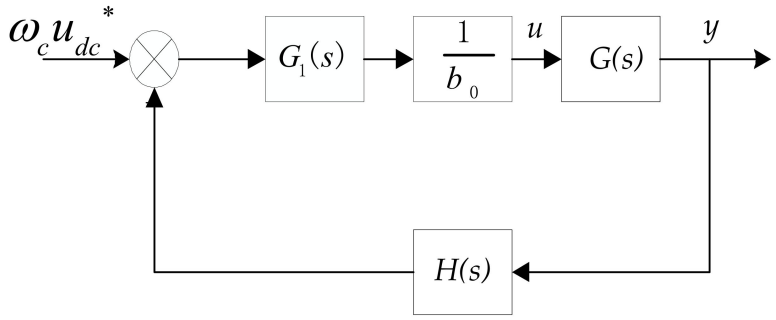

Figure 11. Based on the improved LADRC photovoltaic system voltage outer ring control structure.

The Laplace transform by $f = x_2 = \dot{x}_1 - b_0 u = \dot{y} - b_0 u$ can obtain the following:

$$F(s) = sY(s) - b_0 U(s) \tag{54}$$

Combining this with Figure 11, the closed-loop transfer function of the system is as follows:

$$Y(s) = \frac{s^2 + (2\omega_o + \omega_c)s}{(s+2\omega_o)(s+{\omega_o}^2)(s+\omega_c)} F(s) + \frac{\omega_c}{s+\omega_c} V(s) \tag{55}$$

It can be seen from the above equation that the influence of the disturbance term is only related to ω_o, ω_c, and let $\omega_o = 10$, $\omega_c = 10, 20, 30$ to obtain the amplitude–frequency characteristic curve, as shown in Figure 12; let $\omega_c = 10$, $\omega_o = 10, 20, 30$ can obtain the amplitude–frequency characteristic curve shown in Figure 13. It can be seen from the simulation diagram that increasing ω_o, ω_c can decrease the disturbance and enhance the system's anti-disturbance ability. From the above analysis, it can be seen that the new LADRC has a better ability to suppress disturbances than the traditional LADRC.

When the disturbance f is selected as the unit step signal, the output signal response can be obtained as the following:

$$Y(s) = \frac{a}{(s+\omega_o)} + \frac{a_1}{(s+{\omega_o}^2)} + \frac{a_2}{(s+\omega_c)} \tag{56}$$

$$\begin{cases} a = \frac{\omega_o+\omega_c}{({\omega_o}^2-\omega_o)(\omega_c-\omega_o)} \\ a_1 = \frac{2\omega_o+\omega_c-{\omega_o}^2}{(\omega_o-{\omega_o}^2)(\omega_c-{\omega_o}^2)} \\ a_2 = \frac{2\omega_o}{(\omega_o-\omega_c)({\omega_o}^2-\omega_c)} \end{cases} \tag{57}$$

By performing the inverse Laplace transform on (56), the limit can be found, as follows:

$$\lim_{t\to\infty} y(t) = ae^{-\omega_o t} + a_1 e^{-{\omega_o}^2 t} + a_2 e^{-\omega_c t} = 0 \tag{58}$$

The above analysis shows that the improved LADRC has a good ability to suppress external disturbances, and the larger ω_o, ω_c, the faster the $y(t)$ decay and the shorter the system recovery time.

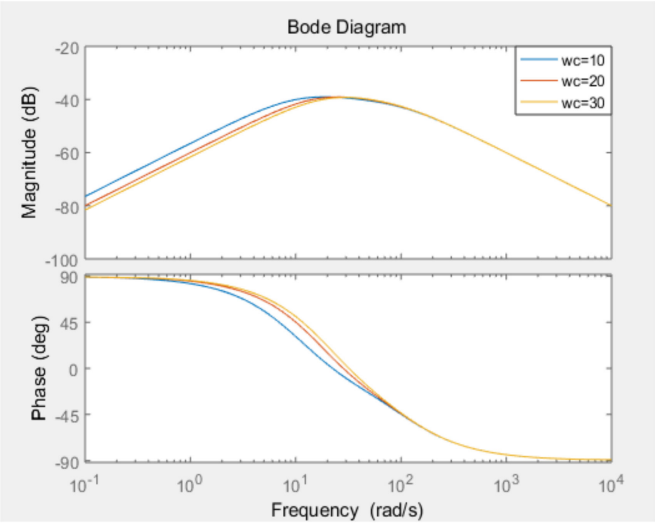

Figure 12. Bode diagram analysis of system disturbance term (ω_c increase).

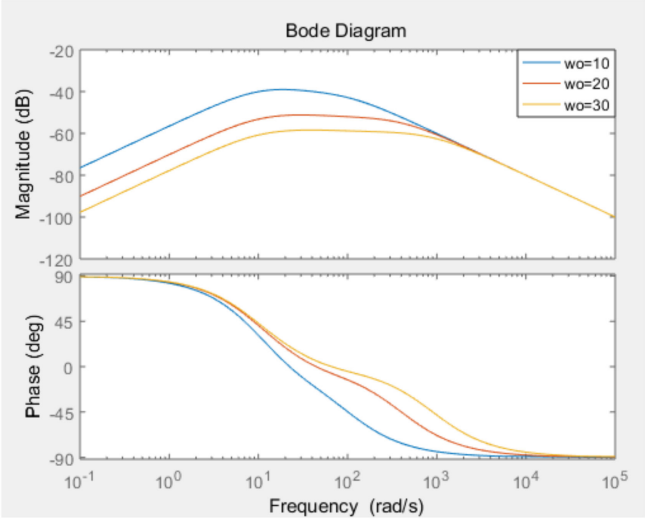

Figure 13. Bode diagram analysis of system disturbance term (ω_o increase).

3.4. New LADRC Tracking Performance Analysis

According to (47), the improved, new LESO has good convergence and can achieve error estimation of system state variables and generalized disturbances. The following further analyzes its dynamic process and tracking performance. When $b_0 = 0$, there are the following:

$$Z_1(s) = K(\frac{1}{s} - \frac{1}{s+\omega_o} + \frac{\omega_o}{(s+\omega_o)^2}) \tag{59}$$

Laplace inverse transformation of (59) can be obtained as follows:

$$z_1(t) = K - K(1-\omega_o t)e^{-\omega_o t}, t \geq 0 \tag{60}$$

The pole of Equation (60) can be found:$t = 2/\omega_o$. Substituting the extreme point into Equation (60) gives the following:

$$z_1(\frac{2}{\omega_o}) = K(1 + e^{-2}) \approx 1.135K \tag{61}$$

LESO can no longer achieve an unbiased estimation of the state variable $x_1(t)(x_1(t) = y(t))$ due to the step mutation of the output signal $y(t)$—that is, $z_1(t) \neq y(t)$, and its error value (0.135 k) is independent of the selection of bandwidth ω_o. In the power system, due to inertia, the output of the controlled object (power) generally does not change abruptly, so LESO will not produce serious errors in tracking the state variable.

4. Stability Analysis of Improved LADRC

4.1. Stability Analysis of Improved Second-Order LESO

The control system is shown in Equation (40). Where x_1 is the system output, $x_1 = y(t)$, $u(t)$ is the control variable, and x_2 is the expansion state variable of the system—that is, the total disturbance of the system. The improved second-order LESO of the above system is constructed as the following:

$$\begin{cases} e_1(t) = z_1(t) - x_1(t) \\ \dot{z}_1(t) = z_2(t) + bu(t) - \eta_1 e_1(t) \\ \dot{z}_2(t) = -\eta_2\left[\dot{e}_1(t) + \eta_1 e_1(t)\right] \end{cases} \tag{62}$$

In the formula,η_1 and η_2 are all parameters greater than zero.

Let $X_1(t) = e_1(t) = z_1(t) - x_1(t)$, $\dot{X}_1 = X_2 = -\eta_1 e_1(t) + e_2(t)$. The available system equations constructed with observation errors are as follows:

$$\begin{cases} \dot{X}_1 = X_2 \\ \dot{X}_2 = -\eta_1\eta_2 X_1 - (\eta_1 + \eta_2)X_2 - h(t) \end{cases} \tag{63}$$

$W = -\eta_1\eta_2(\eta_1 + \eta_2){X_1}^2$ can be constructed according to the Barbach formula:

$$V = -\frac{1}{\Delta}\begin{vmatrix} 0 & {X_1}^2 & 2X_1X_2 & {X_2}^2 \\ 0 & 0 & -\eta_1\eta_2 & 0 \\ 0 & 1 & -\eta_1 - \eta_2 & -\eta_1\eta_2 \\ -\eta_1\eta_2(\eta_1 + \eta_2) & 0 & 1 & -\eta_1 - \eta_2 \end{vmatrix} \tag{64}$$

$$\Delta = \begin{vmatrix} 0 & -\eta_1\eta_2 & 0 \\ 1 & -\eta_1 - \eta_2 & -\eta_1\eta_2 \\ 0 & 1 & -\eta_1 - \eta_2 \end{vmatrix} \tag{65}$$

The Lyapunov function is obtained as the following:

$$V = \eta_1\eta_2(\eta_1\eta_2{X_1}^2 + {X_2}^2) \tag{66}$$

Derivatives can be obtained as follows:

$$\begin{aligned} \dot{V} &= \tfrac{\partial V}{\partial X_1}\dot{X}_1 + \tfrac{\partial V}{\partial X_2}\dot{X}_2 \\ &= -2\eta_1\eta_2(\eta_1 + \eta_2){X_2}^2 - 2\eta_1\eta_2 X_2 h(t) \end{aligned} \tag{67}$$

It can be seen from η_1 and η_2 being positive values that V is positive definite and has an infinite nature. When $h(t) = 0$, there is $\dot{V} < 0$ (X_2 is not always 0). Therefore, the zero point of the LESO error system ($e_1(t) = 0$, $e_2(t) = 0$) is gradually stable over a large range. When the disturbance $h(t) \neq 0$,

the observed value of the system will have a certain error. Suppose $|h(t)| \leq \omega_o$, ω_o is a normal number. After the system reaches steady state, it meets the following:

$$\begin{cases} \dot{X}_1 = \dot{X}_2 = 0 \\ \dot{X}_2 = 0 \end{cases} \tag{68}$$

According to Equations (62) and (63), the steady-state error range can be calculated as the following:

$$|e_1(t)| \leq \frac{\omega_0}{\eta_1 \eta_2} \tag{69}$$

$$|e_2(t)| \leq \frac{\omega_0}{\eta_2} \tag{70}$$

4.2. Stability Analysis of Improved LADRC

From Figure 11, the closed-loop transfer function of the system is as follows:

$$G_c(s) = \frac{\omega_c G_1(s) G(s)/b_0}{1 + G_1(s) G(s) H(s)/b_0} \tag{71}$$

For first-order systems,$y = \frac{f+b_0 u}{s}$, $f = (b - b_0)u(t)$. Then, it can be concluded that

$$y = \frac{1}{s}(b_0 u + (b - b_0)u) \tag{72}$$

From Equation (53), $G_1(s)$, $H(s)$ can be used to obtain the closed-loop transfer function of the system:

$$Y(s) = \frac{(\omega_c s + 2\omega_c \omega_0)(s + {\omega_0}^2)}{a_3 s^3 + a_2 s^2 + a_1 s + a_0} V(s) \tag{73}$$

In the following formula:

$$\begin{cases} a_3 = b_0/b = K_G \\ a_2 = 4{\omega_0}^4 \omega_c + 2{\omega_0}^3 {\omega_c}^2 + {\omega_0}^2 \\ a_1 = a_0/\omega_c + 2\omega_0 \omega_c + {\omega_0}^2 \omega_c \\ a_0 = 2{\omega_0}^3 \omega_c \end{cases} \tag{74}$$

When K_G, ω_o and ω_c are all greater than 0, then the coefficients a_3,a_2,a_1 and a_0 are all greater than 0, and the system stability conditions are as follows:

$$\Delta_3 = \begin{vmatrix} a_2 & a_0 & 0 \\ a_3 & a_1 & 0 \\ 0 & a_2 & a_0 \end{vmatrix} = a_0(a_1 a_2 - a_0 a_3) > 0 \tag{75}$$

This formula represents a stable system—that is, no matter which value b_0 takes, the first-order improved LADRC is stable.

5. Simulation Analysis

In order to verify the feasibility and effectiveness of the above improved ADRC theoretical analysis, a three-phase photovoltaic grid-connected system simulation model was built on the Simulink simulation platform. The model is mainly composed of the following blocks. Photovoltaic(PV) array: the input of this are temperature and irradiance and the output is voltage. This PV array is applied to simulate the actual photovoltaic array. Boost converter: this block is applied to transfer the output voltage of PV array to the designed DC voltage of the two-level converter. The duty cycle of the

switching device in the boost converter is generated by maximum power point tracking (MPPT) control. MPPT block: Applying incremental conductance method to track the maximum power point. Voltage source converter (VSC) controller: This block includes the DC voltage controller and current controller. A phase locked loop (PLL) is applied for synchronization. The DC voltage controller is designed as the new ADRC proposed by this paper. This block is the core segment. Space vector pulse width modulation(SVPWM) is applied to generate the pulse width modulation(PWM) to drive the converter. The control algorithm is chosen as the traditional ADRC and new ADRC. The DC voltages of the converter in different control modes are obtained and compared. The control strategy of the grid-connected inverter is the double closed-loop structure of the voltage outer loop and the current inner loop. Simulation and analysis under various working conditions compare the control effect of the traditional ADRC and the improved ADRC. The parameters in this article are obtained through experience, and the parameters of the system and controller are given in Appendices A and B.

5.1. Comparison of Simulation Graphs of Control Effects under Sudden Changes in Light Intensity

Figure 14 is a comparison diagram of the control effect of the traditional ADRC and improved ADRC under the sudden change in the light intensity, so that the initial value of the DC bus voltage Udc is 500 V, as can be seen from Figure 14a. The light intensity is stepped from 1000 W/m^2 at 0.5 s, changed to 250 W/m^2 and changed from 250 W/m^2 to 1000 W/m^2 at 1 s. The control effects of traditional LADRC and improved LADRC are compared and analyzed by using overshoot and adjustment time. The overshoot index is defined as the maximum deviation from the steady-state voltage and the adjustment time is the time from the beginning to the end of the transient process. It can be seen from Figure 14b,c that during the two sudden changes in light intensity, for Figure 14b, the overshooting of the traditional linear ADRC is 115 V, while that of the improved linear ADRC is 90 V. For adjustment time, the adjustment time of the traditional linear ADRC is 0.08 s, while that of the improved linear ADRC is 0.06 s. For Figure 14c, the overshoot of the traditional LADRC is 20 v, while the overshoot of the improved LADRC is 10 v. For the adjustment time, the traditional LADRC adjustment time is 0.27 s, while the improved LADRC tends to be stable after 0.23 s of adjustment. From these two performance indexes, it can be seen that the improved linear ADRC is correct and accurate and has better control effect. The improved ADRC is less affected by external interference under sudden changes in light intensity, it takes less time to reach steady state, it has better dynamic performance, the DC bus voltage fluctuation range is smaller, and it has better anti-interference performance.

5.2. Contrast and Analysis of Two Control Strategies under Sudden Temperature Change

Figure 15 is a comparison chart of the improved ADRC and traditional ADRC control effects under sudden temperature changes. At 1.5 s, the temperature changes from 25 °C to 75 °C. It can be drawn from the simulation analysis that under the sudden temperature change condition, the overshooting of the traditional linear ADRC is 10 V, while that of the improved linear ADRC is 5 V. For adjustment time, the adjustment time of the traditional linear ADRC is 0.12 s, while that of the improved linear ADRC is 0.09 s. Compared with the traditional LADRC, the improved LADRC can better stabilize the DC bus voltage, it can reach the steady state more quickly, it has better dynamic performance, and the improved LADRC has better anti-interference ability.

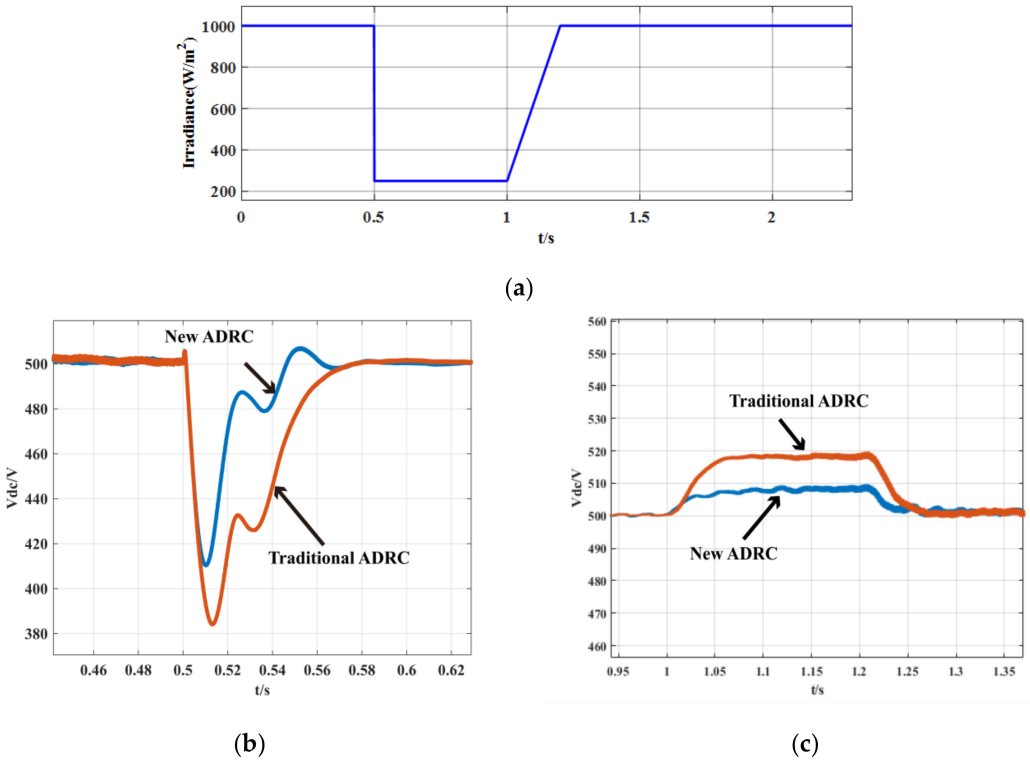

Figure 14. Under the sudden change in light intensity, the voltage waveform comparison between the two control strategies. (**a**) Light intensity change curve; (**b**) The effect of the two control methods when the light intensity drops suddenly; (**c**) The effect of the two control methods when the light intensity rises suddenly.

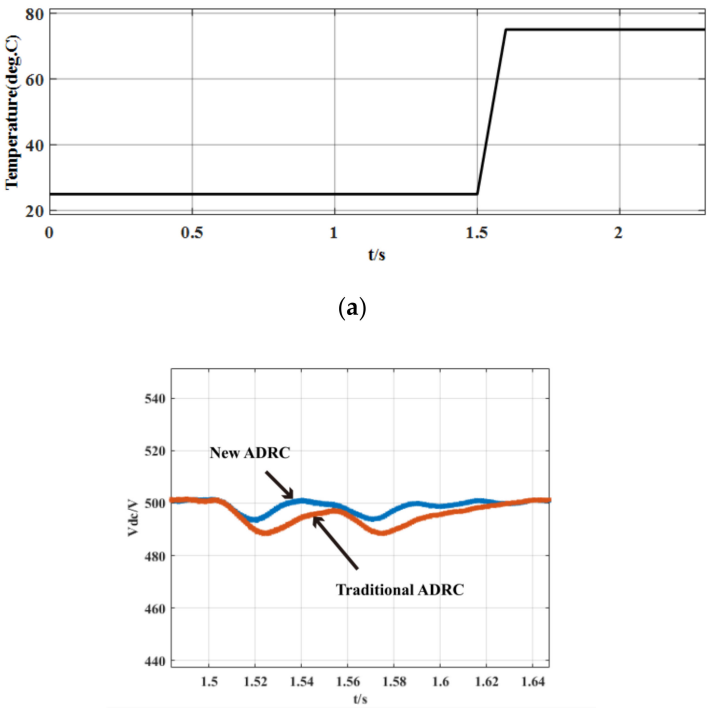

Figure 15. Comparison of DC bus voltage waveform simulation with two control strategies under abrupt temperature conditions. (**a**) Temperature abrupt curve; (**b**) Comparison of control effects of two control strategies under abrupt temperature conditions.

5.3. Comparison of the Effects of Two Control Strategies under Load and Unload Conditions

Figure 16 shows the comparison waveforms of the simulation results of the control effect of the improved ADRC and the traditional ADRC under the conditions of grid load and load reduction (20MW). It can be seen from the simulation diagram that under the condition that the grid is loaded with 20 MW at 2 s and the grid is reduced to 20 MW at 2.3 s, for Figure 16a, the overshooting of the traditional linear ADRC is 16 V, while that of the improved linear ADRC is 13 V. For the adjustment time, the traditional LADRC tends to stabilize after 0.06 s, while the improved LADRC tends to stabilize after 0.03 s. For Figure 16b, the overshooting of the traditional linear ADRC is 12 V, while that of the improved linear ADRC is 10 V. For the adjustment time, the traditional LADRC tends to stabilize after 0.07 s, while the improved LADRC tends to stabilize after 0.03 s. The improved ADRC has a shorter adjustment time, it can reach the steady state faster, the voltage fluctuation range is smaller, and it has better dynamic performance and anti-interference ability.

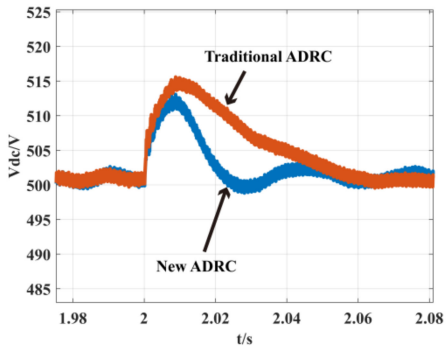

(**a**)

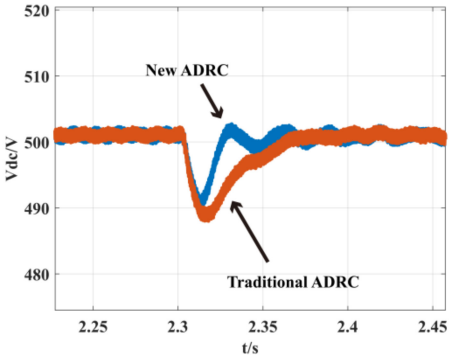

(**b**)

Figure 16. Comparison of simulation graphs of two control strategies under grid load and load reduction conditions. (**a**) Comparison of control effects under grid load conditions; (**b**) Comparison of control effects under grid load reduction conditions.

6. Conclusions

This paper studies the double closed-loop control of the grid-connected inverter of the photovoltaic power generation system. In order to solve the problems of poor stability and susceptibility to external interference of the photovoltaic grid-connected inverter system under the traditional control strategy, this paper innovatively proposes an improved LADRC's double closed-loop control strategy. The linear active disturbance rejection controller (LADRC) can extract the "sum total disturbance" information from the system. The control signal eliminates the disturbance before it has affected the final output of the system. It has a strong ability to suppress internal and external disturbances. The performance of the linear active disturbance rejection controller depends on whether the linear expansion state

observer can estimate the system state variables well. With analysis and optimization based on the traditional LADRC theory, this paper innovatively proposes an improved linear active disturbance rejection controller based on the deviation control principle, which improves the linear expansion state observer's ability to observe system state variables. This improved LADRC takes the new deviation between each state variable and its observation as the adjustment basis of each state variable of the linear expansion state observer (LESO). The improved linear active disturbance rejection controller mentioned in this paper has higher observation accuracy, and the observation value of the total disturbance received by the system is closer to the actual value. The improved LADRC can better observe and eliminate disturbances to the system and has better anti-disturbance performance.

The voltage outer loop is controlled by the improved LADRC. This article first models and analyzes the PV grid-connected inverter. Through the theoretical analysis of the model of photovoltaic grid-connected inverter, the anti-disturbance paradigm of photovoltaic grid-connected inverter is obtained. According to the anti-interference paradigm of photovoltaic inverters, the first-order LADRC is designed and introduced. Based on the traditional LADRC, this paper proposes an improved LADRC. Bode diagram simulation analysis in the frequency domain, this improved method can effectively increase the LESO observation bandwidth, and the phase lag of the middle frequency band has been significantly improved. It can be seen from the simulation diagram that the new LADRC has better noise immunity than the unmodified LADRC. Then, the stability of the improved LADRC is proven. Finally, the control effects of the improved LADRC and the unmodified LADRC are compared and analyzed by changing the light intensity, temperature, grid loading, load reduction and other working conditions. The control performance of traditional LADRC and improved LADRC is analyzed and compared through performance indexes. The simulation results show that the voltage outer loop controller based on the improved LADRC has better dynamic performance, it can quickly reach a steady state, it has stronger ability to suppress disturbances, and it can better stabilize the DC bus voltage and anti-interference performance better than traditional LADRC. This new double closed-loop structure can better stabilize the DC bus voltage and improve the reliability and economy of grid-connected operation, and it has a good reference value for ensuring the safety of the photovoltaic grid-connected system.

According to the results of this research, the problem of parameter optimization of the linear active disturbance rejection controller will be further studied in depth. The traditional empirical method will have limitations and the tuning process is complicated. Next, artificial intelligence technology will be used to optimize the parameters so that the controller will achieve the best control effect in the actual system.

Author Contributions: J.W. is mainly responsible for the theoretical analysis research and simulation and wrote the first draft of the paper on this basis. X.Z. and Y.M. provide theoretical analysis guidance and overall revision of the paper. All authors have read and agreed to the published version of the manuscript.

Funding: This work was funded by the National Natural Science foundation of China (NO.51877152) and Natural Science Foundation of Tianjin of China (NO.18JCZDJC97300).

Acknowledgments: The authors are grateful for the support of the National Natural Science Foundation of China (NO. 51877152), Natural Science Foundation of Tianjin of China (NO. 18JCZDJC97300) and Tianjin University of Technology.

Conflicts of Interest: The authors declare no conflict of interest.

Abbreviations

Acronym	Definition
LESO	Linear extended state observer
LSEF	Linear state error feedback
LTD	Linear tracking differentiator
LADRC	Linear active disturbance rejection controller

Appendix A

Table A1. Parameters of three-phase photovoltaic grid-connected inverter.

Parameter	Value	Unit
DC bus voltage	500	V
Grid line voltage	380	V
Filter inductance	1885	μH
Grid frequency	60	Hz
DC capacitance	0.012	F

Appendix B

Table A2. Controller parameters.

Controller Parameters	Value
Controller Bandwidth ω_c	439.8
Observer Bandwidth ω_o	1759.3
Control gain b_0	12,000

References

1. Tafti, H.D.; Maswood, A.I.; Konstantinou, G.; Townsend, C.D.; Acuna, P.; Pou, J. Flexible control of photovoltaic grid-connected cascaded H-bridge converters during unbalanced voltage sags. *IEEE Trans. Ind. Electron.* **2018**, *65*, 6229–6238. [CrossRef]
2. Huenteler, J.; Niebuhr, C.; Schmidt, T.S. The effect of local and global learning on the cost of renewable energy in developing countries. *J. Clean. Prod.* **2016**, *128*, 6–21. [CrossRef]
3. Wu, W.; Liu, Y.; He, Y.; Chung, H.S.H.; Liserre, M.; Blaabjerg, F. Damping Methods for Resonances Caused by LCL-filter-based Current-controlled Grid-tied Power Inverters: An Overview. *IEEE Trans. Ind. Electron.* **2017**, *64*, 7402–7413. [CrossRef]
4. Hu, H.; Harb, S.; Kutkut, N.; Batarseh, I.; Shen, Z.J. A Review of Power Decoupling Techniques for Microinverters with Three Different Decoupling Capacitor Locations in PV Systems. *IEEE Trans. Power Electron.* **2013**, *28*, 2711–2726. [CrossRef]
5. Duman, T.; Marti, S.; Moonem, M.; Abdul Kader, A.; Krishnaswami, H. A Modular Multilevel Converter with Power Mismatch Control for Grid-Connected Photovoltaic Systems. *Energies* **2017**, *10*, 698. [CrossRef]
6. Siddiqui, R.; Kumar, R.; Jha, G.K.; Gowri, G.; Morampudi, M.; Rajput, P.; Raghava, S.S. Comparison of different technologies for solar PV (Photovoltaic) outdoor performance using indoor accelerated aging tests for long term reliability. *Energy* **2016**, *107*, 550–561. [CrossRef]
7. Bianchini, A.; Gambuti, M.; Pellegrini, M.; Saccani, C. Performance analysis and economic assessment of different photovoltaic technologies based on experimental measurements. *Renew. Energy* **2016**, *85*, 1–11. [CrossRef]
8. Tossa, A.K.; Soro, Y.M.; Thiaw, L.; Azoumah, Y.; Sicot, L.; Yamegueu, D.; Razongles, G. Energy performance of different silicon photovoltaic technologies under hot and harsh climate. *Energy* **2016**, *103*, 261–270. [CrossRef]
9. Guo, X.; Liu, W.; Lu, Z. Flexible Power Regulation and Current-limited Control of Grid-connected Inverter under Unbalanced Grid Voltage Faults. *IEEE Trans. Ind. Electron.* **2017**, *64*, 7425–7432. [CrossRef]
10. Liao, C.Y.; Lin, W.S.; Chen, Y.M.; Chou, C.Y. A PV Micro-inverter with PV current decoupling strategy. Title of the article. *IEEE Trans. Power Electron.* **2017**, *32*, 6544–6557. [CrossRef]
11. Liu, X.R.; Gao, C.; Wang, Z.L. A Nonlinear Disturbance Observer Based DC-bus Voltage Control for PV Grid-connected Inverter. *Power Syst. Tech.* **2019**, *5*, 1–11.
12. Xu, X.Y. *Research on Control Strategy of Grid Side Inverter for Wind Power*; North China Electric Power University: Beijing, China, 2017.

13. Carli, R.; Dotoli, M. A decentralized resource allocation approach for sharing renewable energy among interconnected smart homes. In Proceedings of the 54th IEEE Conference on Decision and Control (CDC), Osaka, Japan, 15–18 December 2015; pp. 5903–5908. [CrossRef]
14. Zhang, Y.; Gatsis, N.; Giannakis, G.B. Robust Energy Management for Microgrids With High-Penetration Renewables. *IEEE Trans. Sustain. Energy* **2013**, *4*, 944–953. [CrossRef]
15. Kerdphol, T.; Rahman, F.S.; Mitani, Y.; Watanabe, M.; Küfeoğlu, S.K. Robust Virtual Inertia Control of an Islanded Microgrid Considering High Penetration of Renewable Energy. *IEEE Access* **2018**, *6*, 625–636. [CrossRef]
16. Buticchi, G.; De Carne, G.; Barater, D.; Zou, Z.; Liserre, M. Analysis of the frequency-based control of a master/slave micro-grid. *Power Electron. IET* **2017**, *10*, 1570–1576. [CrossRef]
17. Long, B.; Wang, W.; Huang, L.J.; Chen, Y.; Li, F.S.; Sun, H.B.; Li, H. Design and implementation of a virtual capacitor based DC current suppression method for grid-connected inverters. *ISA Trans.* **2019**, *92*, 257–272. [CrossRef]
18. Seyyedzadeh, S.M.; Shoulaie, A. Accurate Modeling of the Nonlinear Characteristic of a Voltage Source Inverter for Better Performance in Near Zero Currents. *IEEE Trans. Ind. Electron.* **2018**, *66*, 71–78. [CrossRef]
19. Sun, Z.N.; Wang, D.Z.; Yuan, T.Q.; Liu, Z.R.; Yu, J.H. A Novel Control Strategy for Grid-Connected Inverter Based on Iterative Calculation of Structural Parameters. *Energies* **2018**, *11*, 3306. [CrossRef]
20. Zhang, R.P.; Chen, Z.Q. PI parameter setting of voltage type PWM rectifier. *Chin. J. Power Sources* **2014**, *38*, 941–942. [CrossRef]
21. Liu, S.R.; Yang, P.; Xiao, Y. Algorithm research of deadbeat control for double-stage photovoltaic grid-connected inverter. *Power Syst. Prot. Control* **2010**, *38*, 26–29.
22. Wang, Y.S.; Wang, S.Y.; Hai, R. Control strategy for grid-connected inverter to suppress harmonics based on PR regulator. *Chin. J. Power Sources* **2016**, *40*, 184–188.
23. Teng, G.F.; Xiao, G.C.; Zhang, Z.B. A single-loop current control method for LCL-filtered grid-connected inverters based on the repetitive controller. *Proc. CSEE* **2013**, *33*, 13–21.
24. Han, J. From PID to Active Disturbance Rejection Control. *IEEE Trans. Ind. Electron.* **2009**, *56*, 900–906. [CrossRef]
25. Zubing, Z.; Lijuan, C.; Huixia, G. The Application of Auto-Disturbance Rejection Controller for Voltage Source PWM Inverter. *Trans. China Electrotech. Soc.* **2004**, *19*, 84–88.
26. Yang, L.; Zeng, J.; Ma, W.; Huang, Z. Voltage control of micro-grid inverter based on improved second order linear active disturbance rejection technology. *Autom. Electr. Power Syst.* **2019**, *43*, 215–227.
27. Liu, L.; Xu, Z.; Mei, Q. Induction Motor Drive System Based on the Flux Observer LESO and LADRC. *Congr. Intell. Syst. IEEE* **2009**, *2*, 248–252.
28. Ding, Z.; Liu, B.; Zhang, Y. Optimal Control for DC Side Voltage of Active Power Filter Based on Auto-Disturbance Rejection Control. *Power Syst. Technol.* **2013**, *37*, 2030–2034.
29. Li, J.; Qi, X.; Xia, Y.; Gao, Z. On linear/nonlinear active disturbance rejection switching control. *Acta Autom. Sin.* **2016**, *42*, 202–212.
30. Gao, Z.Q. Scaling and bandwidth—Parameterization based controller tuning. In Proceedings of the American Control Conference, Denver, CO, USA, 4–6 June 2003; pp. 4989–4996.
31. Zhan, L.; Liu, Y.; Liu, Y. A Clarke Transformation-Based DFT Phasor and Frequency Algorithm for Wide Frequency Range. *IEEE Trans. Smart Grid* **2018**, *9*, 67–77. [CrossRef]
32. Faisal, M.; Alam, M.S.; Arafat, M.I.M.; Rahman, M.M.; Mostafa, S.M.G. PI controller and park's transformation based control of dynamic voltage restorer for voltage sag minimization. In Proceedings of the 9th International Forum on Strategic Technology (IFOST), Cox's Bazar, Bangladesh, 21–23 October 2014; pp. 276–279. [CrossRef]
33. Irannezhad, F.; Hosseinian, S.H.; Abedi, M.; Vahidi, B. Using the Instantaneous Power Theory in order to control the current in the parallel active filter to compensate reactive power and reduction of harmonics. In Proceedings of the IEEE International Conference on Power Electronics, Drives and Energy Systems (PEDES), Bengaluru, India, 16–19 December 2012; pp. 1–5. [CrossRef]

34. Talarico, C.; D'Amato, G.; Coviello, G.; Avitabile, G. A high precision phase control unit for DDS-based PLLs for 2.4-GHz ISM band applications. In Proceedings of the IEEE 58th International Midwest Symposium on Circuits and Systems (MWSCAS), Fort Collins, CO, USA, 2–5 August 2015; pp. 1–4. [CrossRef]
35. D'Amato, G.; Avitabile, G.; Coviello, G.; Talarico, C. A beam steering unit for active phased-array antennas based on FPGA synthesized delay-lines and PLLs. In Proceedings of the International Conference on Synthesis, Modeling, Analysis and Simulation Methods and Applications to Circuit Design (SMACD), Istanbul, Turkey, 7–9 September 2015; pp. 1–4. [CrossRef]



© 2020 by the authors. Licensee MDPI, Basel, Switzerland. This article is an open access article distributed under the terms and conditions of the Creative Commons Attribution (CC BY) license (http://creativecommons.org/licenses/by/4.0/).